Research paper

Magnetic coupling constants for MnO as calculated using hybrid density functional theory

Andrew J. Logsdail [a,b,*], Christopher A. Downing [a,c], C. Richard A. Catlow [a,b,d], Alexey A. Sokol [a]

[a] Kathleen Lonsdale Materials Chemistry, Department of Chemistry, University College London, 20 Gordon Street, London WC1H 0AJ, United Kingdom
[b] Cardiff Catalysis Institute, School of Chemistry, Cardiff University, Cardiff CF10 3AT, United Kingdom
[c] Scientific Computing Department, STFC Daresbury Laboratory, Daresbury, Warrington WA4 4AD, United Kingdom
[d] UK Catalysis Hub, Research Complex at Harwell, Science and Technology Facilities Council Rutherford Appleton Laboratory, Harwell Science and Innovation Campus, Oxon OX11 0QX, United Kingdom

ARTICLE INFO

ABSTRACT

The properties of MnO have been calculated using generalised gradient approximation (GGA-) and hybrid (h-) density functional theory (DFT), specifically variants of the popular PBE and PBESol exchange–correlation functionals. The GGA approaches are shown to be poor at reproducing experimental magnetic coupling constants and rhombohedral structural distortions, with the PBESol functional performing worse than PBE. In contrast, h-DFT results are in reasonable agreement with experiment. Calculation of the Néel temperatures using the mean-field approximation gives overestimates relative to experiment, but the discrepancies are as low as 15 K for the PBE0 approach and, generally, the h-DFT results are significant improvements over previous theoretical studies. For the Curie–Weiss temperature, larger disparities are observed between the theoretical results and previous experimental results.
© 2017 The Authors. Published by Elsevier B.V. This is an open access article under the CC BY license (http://creativecommons.org/licenses/by/4.0/).

1. Introduction

Transition metal oxides (TMOs) are popular materials for studying fundamental physical properties because of their relative structural simplicity and intriguing magnetic behaviour, where a transition from paramagnetic to antiferromagnetic (AFM) ordering occurs below their respective Néel temperature (T_N) [1]. MnO is a classic representation of the family of first row TMOs: at room temperature, it is paramagnetic (PM) and adopts a cubic structure with a lattice constant (a) of 2.223 Å [2–4]; short-range magnetic ordering occurs below the Curie–Weiss temperature (θ) of ~ 550 K [5] and then, below the T_N of 118 K [6], MnO adopts a long-range ordered AFM spin configuration [7]. The AFM configuration is with the magnetic moments of the d^5 valence electrons on the Mn^{2+} cations aligned in parallel along the diagonal (1 1 1) plane [7], with small modulated out-of-plane components recently identified using total neutron scattering [8]. The AFM spin configuration results in a small rhombohedral-type distortion:

the unit cell angle, α, is reported as being 90.60–90.62°, with an accompanying a of 2.215–2.216 Å [9–11], though Goodwin et al. highlight that the distortion cannot be truly rhombohedral due to symmetry constraints [8].

Insight into the fundamental properties of TMOs, such as spin configuration and associated coupling constants, is aided by computational simulations; however, MnO has a long-standing reputation of being a challenge to simulate using modern density functional theory (DFT) due to strong on-site Coulomb repulsion by the 3d states [12–14]. At the local and semi-local level of DFT, such as the local density approximation (LDA) and generalised gradient approximation (GGA), problems exist due to the inadequacy of the exchange–correlation (XC) functionals at localising the valence d electrons [15–17], partly due to inherent self-interaction errors [18–20], which leads to underestimation of the electronic band gap. MnO is considered a prototypical Mott–Hubbard insulator with a key d-d intra-atomic Coulomb repulsion. Attempts to use on-site Coulomb-repulsion corrected DFT, namely DFT + U, have shown promise in simultaneously reproducing experimental structures, electronic band gaps and, for MnO, spin coupling constants [21–24], though the empirical parameterisation of this approach leaves scope for technical improvements. A more

robust *ab initio* solution is the use of hybrid-DFT (h-DFT), where a fraction of the exchange energy in the density functional is replaced with Hartree–Fock (HF) exact exchange [25,26]. In h-DFT, the explicit two-electron consideration of electron–electron interactions, rather than the mean-field approach of DFT, means that the localisation of electrons is improved, which typically leads to better agreement with experiment, compared to GGA approaches, for a range of materials and properties [22,26,27]. However, the accuracy of h-DFT comes with an additional computational overhead that increases computation time by an order of magnitude, relative to traditional DFT, and so justification for using h-DFT must be made carefully.

To compare systematically different levels of DFT theory when studying the properties of MnO, one can consider the energetics of the several competing low-temperature magnetic configurations: the relative energy differences between spin configurations can be used to derive observables such as T_N and θ. The AFM configuration of MnO, where neighbouring cations have some of their spins anti-aligned as shown in Fig. 1, can take one of two forms: AFM(I), as shown in Fig. 1A, where the unpaired electrons on each cation are aligned ferromagnetically along one primary crystallographic plane, e.g. (1 0 0), but anti-parallel between adjacent planes; or AFM(II), as shown in Fig. 1B, where the unpaired electrons on each cation are aligned ferromagnetically along a diagonal plane, e.g. (1 1 1), and anti-parallel again between adjacent planes [13]. Alternatively, in a ferromagnetic (FM) spin configuration, the unpaired electrons are aligned across all cation centres. Experiment has only identified the AFM(II) phase at low-temperature, whilst calculations have confirmed the hierarchy of energetic ordering for these different spin configurations, placing the AFM (II) and AFM(I) phases lower in energy than the FM or PM arrangements [12,22,24,27,28].

In this work, we build on previous computational investigations by calculating and comparing the magnetic coupling constants and transition temperatures for MnO using several popular exchange–correlation (XC) density functionals of similar theoretical origins, specifically considering a recent reparameterisation for solid-state materials and contrasting this to the original derivation made using free atom assumptions. Our results are obtained by calculating the energy differences between the various spin configurations, as outlined in Section 2, and these data are used to parameterise a Heisenberg Hamiltonian with which coupling constants and transition temperatures can be derived. The results are presented in

Section 3, and Section 4 concludes with comments as to the observed strengths and weaknesses of the methods presented.

2. Methodology

Calculations were performed using a periodic planewave methodology, as implemented in the VASP software package [29–31], with a planewave cutoff of 900 eV and the projector augmented wave (PAW) representation for the core electrons. A Γ-point-centred **k**-grid of $9 \times 9 \times 9$ was used for the FM and AFM(I) calculations, which respectively contained 2 and 8 atoms (N) in the unit cell, and a **k**-grid of $5 \times 5 \times 5$ was used for the larger AFM(II) calculation ($N = 16$); these grids correspond to a well converged reciprocal-space sampling of one **k**-point per 0.04 Å^{-1} (or less). A convergence threshold of 10^{-8} eV was used for the self-consistent field cycle. Calculations were performed initially using the PBE and PBE0 XC functionals [32,33], before complementing these with studies using the solid-state reparameterised version of the PBE XC functional, namely PBESol [34], as well as its hybrid equivalent, PBESol0, where 25% exact exchange is included in the place of the GGA exchange [25,33].

To calculate equations of state for each magnetic configuration, single point calculations were performed for fixed unit cells with internal bond angles set to 90° (i.e. cubic) and either FM, AFM(I) or AFM(II) spin configurations. The cohesive energy per atom, E_{coh}, is calculated for each spin configuration as:

$$E_{coh} = \frac{E_{tot}}{N} - \frac{\left(E_{atom}^{Mn} + E_{atom}^{O}\right)}{2} \tag{1}$$

with E_{tot}, E_{atom}^{Mn} and E_{atom}^{O} corresponding to either the total energy of the FM, AFM(I) or AFM(II) unit cells, the energy of the gas-phase Mn atom and the energy of the gas-phase O atom, respectively. In order to validate the accuracy of using differing unit cells for differing spin configurations, E_{coh} was calculated for FM and AFM(I) magnetic orderings using the PBE XC functional with the $N = 16$ unit cell and compared to the results for the reduced-size unit cells: differences of < 0.1 meV and < 0.6 meV were respectively calculated, justifying our approach. Internal geometry and stress tensor optimisation were used, where discussed, with a convergence criteria of 0.001 eV Å^{-1} for forces. Collinear spin was used throughout.
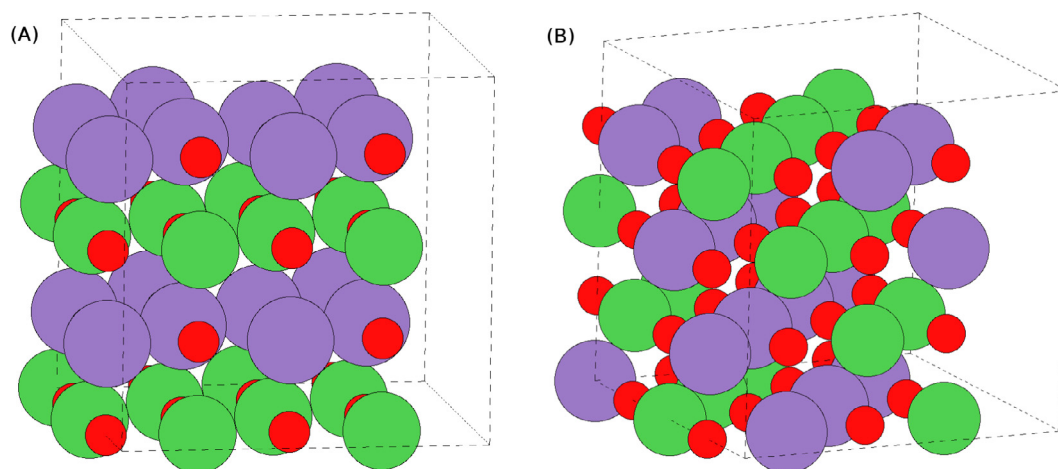
Fig. 1. Magnetic ordering for antiferromagnetic spin configurations: (A) AFM(I), with spins aligned on the horizontal (1 0 0) axis and anti-parallel on the vertical axis; (B) AFM (II), with the spins aligned on the diagonals (1 1 1) axis and anti-parallel perpendicular to this. Purple and green spheres represent manganese cations with spin-up and spin-down configurations; red spheres are the anionic oxygen species. (For interpretation of the references to colour in this figure legend, the reader is referred to the web version of this article.)

3. Results

Equations of state (E_{coh} vs. a) for the FM, AFM(I) and AFM(II) spin configurations in the *cubic* MnO phase are presented in Figs. 2 and 3 for GGA and hybrid-DFT methods, respectively. The lowest energy spin configuration is AFM(II) in all cases, with a parabolic fit of the data points giving an optimal a of 2.219, 2.186, 2.215 and 2.193 Å when using the PBE, PBESol, PBE0 and PBESol0 XC functionals. The observations for PBE and PBE0 are comparable with previous results of Schrön et al. (2.221 Å) and Franchini et al. (2.22 Å) [22,24]. The structural differences are observed as varying marginally between XC functional choices, but the PBE XC functionals clearly result in larger a than PBESol. The PBE results are closer to experiment, which is reported as being 2.2155 ±0.0005 Å. In addition, it is noted that PBESol-based XC functionals give E_{coh} as being ~0.4 eV lower than for the PBE-family of XC functionals.

For comparison, $a = 2.216$, 2.178, 2.213 and 2.191 Å for the same respective XC functionals in the stress-tensor optimised *rhombohedral* unit cell, as measured by the bond distance between an Mn and a nearest neighbour O atom, and an internal angle (α) of 91.63, 92.36, 90.91 and 91.02°, as measured between an Mn, a nearest neighbour O and a next nearest neighbour same-spin Mn atom; the optimised unit cells are provided in the Supporting Information (SI). In all cases, there is a very small contraction of a, relative to the cubic models, with a biggest change of 0.008 Å for PBESol. Overall, h-DFT gives the smallest rhombohedral distortions and the PBE (PBE0) result is comparable with previous computational reports of $\alpha = 91.66$ and 91.75° ($\alpha = 90.88°$) [22,24]. Furthermore, a is closest to experiment ($a = 2.2155 \pm 0.0005$ Å)

when using PBE, whilst α is closest for PBE0 ($\alpha = 90.60 - 90.62°$) [9–11], with the remaining difference of 0.2° perhaps attributable to low-temperature thermal effects neglected in our simulations. We associate the size of the rhombohedral distortions to the interaction between neighbouring Mn cations with the spins aligned and anti-aligned: for PBESol, the distance between same-spin cations is 3.141 Å and then 3.021 Å between spin anti-aligned cations; in comparison, for PBESol0 the respective values are 3.125 and 3.07 Å i.e. the repulsion (attraction) between parallel (anti-parallel) spin is exaggerated by GGA methods. Despite the structural differences discussed for cubic and rhombohedral unit cells, the difference in E_{coh} between these two structures is < 7 meV for AFM(II) spin configurations using the PBESol XC functional, and lower still for all other XC functionals, which shows the importance of high numerical accuracy when modelling these systems.

The coupling constants J_1 and J_2, which are respectively associated with nearest neighbour (NN) and next-nearest neighbour (NN) spin coupling as shown in Fig. 4, can be calculated by comparing the relative energies of the different magnetic configurations. Taking the Heisenberg Hamiltonian and neglecting the longitudinal and transverse spin fluctuations, one gets a generalised Ising model with matrix components [24]:

$$H_i = \sum_{l=1,2} (z_l^{\uparrow\uparrow} - z_l^{\uparrow\downarrow}) J_l S_i S_l \tag{2}$$

where H_i is the matrix element for atom i, index l runs over all the shells of NN (1) and NNN (2) atoms, S_i and S_l are the corresponding spins of the indexed atoms, J_l is the coupling constant between atom i and each atom in shell l, and $z_l^{\uparrow\uparrow}$ and $z_l^{\uparrow\downarrow}$ denote the number
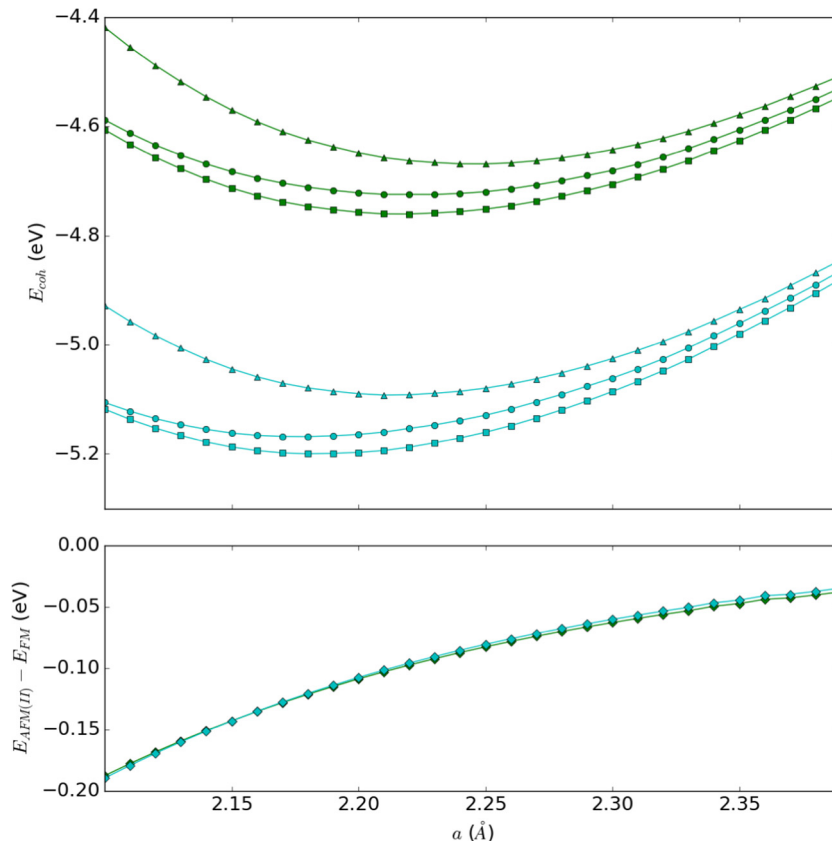
Fig. 2. Energetics of different magnetic configurations as a function of lattice constant, as calculated for MnO using the GGA density functionals: PBE and PBESol are coloured green and aqua, respectively. The top graph gives the cohesive energy (E_{coh}) per atom when using the FM, AFM(I) and AFM(II) magnetic configurations, as represented by triangles, circles and squares, respectively, and the bottom graph displays the energy difference between the AFM(II) and FM phases (diamond symbols). Energies are in eV, with the lattice constant given in Å. (For interpretation of the references to colour in this figure legend, the reader is referred to the web version of this article.)
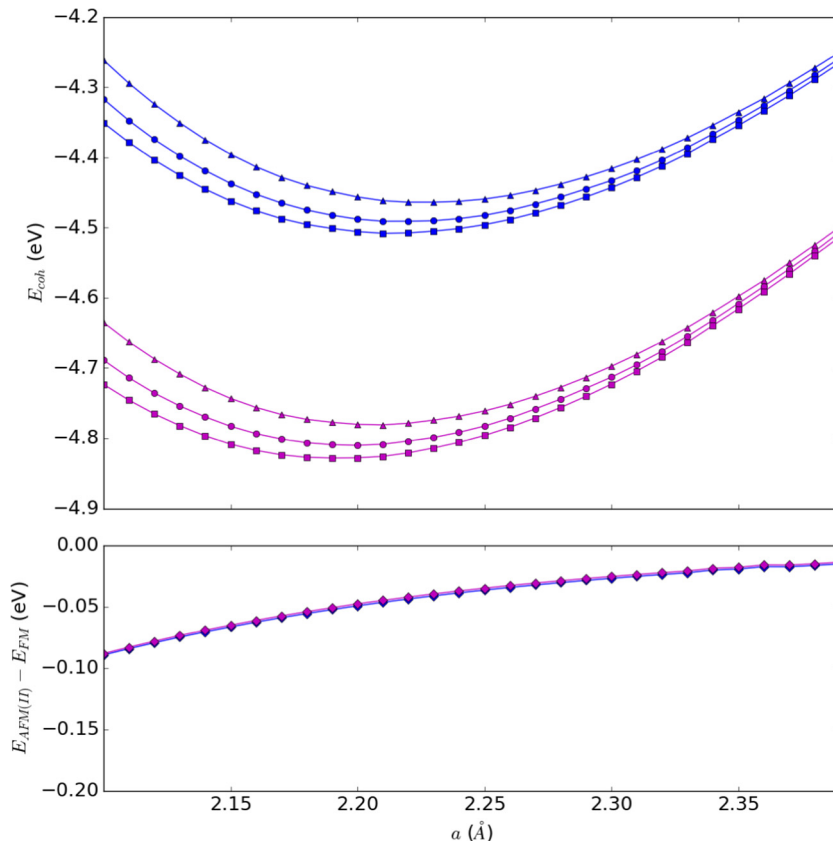
Fig. 3. Energetics of different magnetic configurations as a function of lattice constant, as calculated for MnO using the hybrid density functionals: PBE0 and PBESol0 are coloured blue and purple, respectively. The top graph gives the cohesive energy (E_{coh}) per atom when using the FM, AFM(I) and AFM(II) magnetic configurations, as represented by triangles, circles and squares, respectively, and the bottom graph displays the energy difference between the AFM(II) and FM phases (diamond symbols). Energies are in eV, with the lattice constant given in Å. (For interpretation of the references to colour in this figure legend, the reader is referred to the web version of this article.)
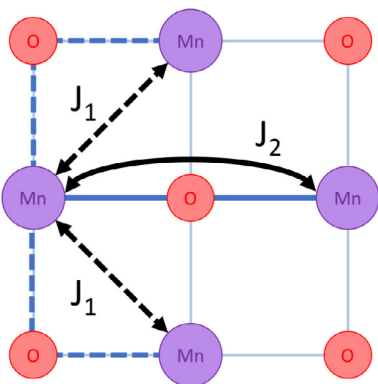
Fig. 4. Illustration of the interactions represented by coupling constants between Mn cations (purple circles). J_1 (black dashed arrow), relates to the strength of interaction between nearest neighbour cation species, with coupling through an adjoining oxygen (red circles) at a bond angle of ~90° (blue dashed line). J_2 (black solid arrow), relates to the strength of interaction between next-nearest neighbour cation species, with coupling through an adjoining oxygen at a bond angle of ~180° (blue solid line). (For interpretation of the references to colour in this figure legend, the reader is referred to the web version of this article.)

tions, where the spin densities are summed within the defined Wigner Seitz radii (r_s). Both definitions have been considered here, with the DFT-calculated S taken from the results using the lowest-energy AFM(II) unit cell with $r_s = 1.164$ Å, as defined by the chosen PAW configuration. The calculated magnetic moments, μ (= 2S) are 4.17, 4.11, 4.37 and 4.35 μ_B for the *rhombohedral* unit cells when using PBE, PBESol, PBE0 and PBESol0 XC functionals, respectively; identical values of μ are calculated for the *cubic* unit cell. Table 1 shows μ is 0.2 μ_B compared to previous calculations, which could be attributable to our choice of r_s. Illustrations showing variation in μ with respect to unit cell volume and spin ordering are provided in the SI.

By considering the differing quantities of spin-equivalent and spin-inequivalent NN and NNN in FM, AFM(I) and AFM(II) spin configurations, J_1 and J_2 can be derived from Eq. (2) as [13,28]:

$$J_1 = \frac{E_{FM} - E_{AFM(I)}}{8S^2 k_B} \tag{3}$$

$$J_2 = \frac{E_{FM} - E_{AFM(II)}}{6S^2 k_B} - J_1 \tag{4}$$

where the energy per formula unit (eV) of the FM, AFM(I) and AFM(II) phases is denoted as $E_{FM}, E_{AFM(I)}$ and $E_{AFM(II)}$, respectively, and division by the Boltzmann constant ($k_B = 0.086173$ meV K^{-1}) converts to the traditional units of K. With this choice of Hamiltonian, positive and negative values of J correspond to energy gain for anti-parallel and parallel spin configurations, respectively.

of neighbours in each shell l with spins aligned parallel and anti-parallel to atom i, respectively. It is noted that our definition of H_i does not contain a double summation, hence removing a factor of 1/2 seen elsewhere in the literature [24]. There is a high-spin d^5 electron configuration on each Mn^{2+} cation, thus the formal definition of S is 5/2; one can alternatively derive S from the DFT calcula-

Table 1

Calculated magnetisation of the Mn^{2+} cation (μ), coupling constants (J_1 and J_2), Néel Temperatures (T_N) and Curie constants (θ), given in **bold**, compared against previous literature (PBE, h-DFT and HF). μ is given in units of μ_B, with all other values in K. T_N and θ given in *italics* have been calculated by inserting J_1 and J_2 into Eqs. (5) and (6), and are given in parentheses if accompanying a previously reported result; values marked with ∗ were calculated using $S = \mu/2$, rather than the formal definition of $S = 5/2$. [a] Original value multiplied by 2, as considered elsewhere [14,24]. [b] Calculated via Monte Carlo simulations. [c] Calculated via Mean Field Theory.

Method	[Ref]	μ	J_1	J_2	T_N	θ
Exp.	[35]	4.54	–	–	–	–
Exp.	[36]	–	10	11	*192.5*	*540*
Exp.	[37]	–	8.47[a]	9.63[a]	*170.59*	*476.01*
Exp.	[38]	–	9	10.4	*180.74*	*493.48*
Exp.	[6]	–	–	–	116	610
Exp.	[9]	–	–	–	120	425.4
Exp.	[39]	–	–	–	116	461
TB	[13]	–	16.36	4.04	*141.4*	*643.3*
PBE	[22]	4.31	17.6	27.9	*488.25*	*1104.25*
PBE	[24]	4.3	15.09	27.85	*487.39*	*1015.40*
PBE∗	[24]	4.3	19.73	38.29	*520 (518.70)*	*1060 (1053.13)*
PBE	[14]		17.64	27.67	*249[b] (373.26)*	*849.23*
PBE		**4.17**	**14.32**	**15.89**	**278.06**	**779.33**
PBE∗		**4.17**	**20.62**	**22.88**	**293.94**	**823.84**
PBESol		**4.11**	**20.69**	**16.66**	**291.63**	**1015.63**
PBESol∗		**4.11**	**30.64**	**24.69**	**309.72**	**1078.64**
PBE + U	[22]	4.69	8.2	4.3	*75.25*	*362.25*
PBE + U	[24]	4.59	11.60	11.60	*203.08*	*609.24*
PBE + U∗	[24]	4.59	13.93	13.93	*210 (210.61)*	*630 (631.83)*
PBE + U	[40]		10.40	5.20	*90.98*	*454.90*
PBE + U	[40]		10.58[c]	9.65[c]	*168.96*	*539.38*
B3LYP	[28]	4.73	9.8	20.5	*358.75*	*701.75*
PBE0	[22]	4.52	11.5	13.7	*239.75*	*642.25*
HSE03	[24]	4.53	13.93	12.76	*223.39*	*710.78*
HSE03∗	[24]	4.53	16.25	15.09	*230 (223.13)*	*720 (703.71)*
HSE06	[14]		13.00	14.48	*125[b] (253.44)*	*708.34*
PBE0		**4.37**	**6.79**	**7.59**	**132.83**	**370.54**
PBE0∗		**4.37**	**8.90**	**9.94**	**138.31**	**385.83**
PBESol0		**4.35**	**7.38**	**8.36**	**146.24**	**404.52**
PBESol0∗		**4.35**	**9.76**	**11.05**	**152.51**	**421.86**
HF	[41]	4.92	–	–	*94*	–
HF	[22]	4.7	2.7	4.3	*75.25*	*169.75*

The calculated coupling constants are presented in Table 1: for PBE, we obtain $J_1 = 14.32$ and $J_2 = 15.89$ K, whereas for PBESol, $J_1 = 20.69$ and $J_2 = 16.66$ K. The results for J_1 are similar to previous PBE calculations (15.09–19.73 K), whereas J_2 is noticeably smaller (27.67–38.29 K). Improvements in J_2 are made if $S = 5/2$ is replaced with $S = \mu/2$, although this also raises J_1. Testing of the planewave cutoff illustrates that this is not the cause of discrepancy (Table 1, SI). Thus, as J_1 is dependent on E_{FM} and $E_{AFM(I)}$, the discrepancy of J_2 with respect to previous results is most likely attributable to differences in $E_{AFM(II)}$: as an example, a decrease in E_{coh} of 10 meV leads to an increase of 3.1 K for J_2 for the PBE XC functional. For h-DFT, J_1 and J_2 are calculated respectively as being 6.79 and 7.59 K for PBE0, and 7.38 and 8.35 K for PBESol0: these results are much closer to experiment ($J_1 = 8.47 - 10$ K; $J_2 = 9.63 - 11$ K) than those of the GGA. However, the results are again lower than previously reported PBE0 calculations ($J_1 = 11.5$ K; $J_2 = 13.7$ K) though, in this instance, *both* our J_1 and J_2 values are reduced compared to previous reports. This is different to the GGA results and implies an influence of E_{FM} and/or $E_{AFM(II)}$: an increase of E_{coh} by 10 meV for the FM configuration raises J_1 and J_2 by 2.32 and 0.77 K, respectively, when using our PBE0 results. It is noted also that the error on reported experimental results is not insignificant: ±10% from Lines et al. [36], ±3.5% from Pepy [37] and ±3% from Koghi et al. [38].

Clearly, the localisation of the d electrons is key to decreasing the coupling constants, which is consistent with previous work: [12] the generalised gradient approximation (GGA), with 0% exact exchange, has previously given $J_1 = 15.9 - 17.6$ and $J_2 = 27.85 - 27.9$ K (PBE) [22,24], whilst HF calculations, with 100% exact exchange, gave $J_1 = 2.7$ and $J_2 = 4.3$ [22]. The parameterised PBE + U and unparameterised h-DFT approaches, with the latter typically containing ∼ 25% exact exchange, give intermediates to these extremes: $J_1 = 11.5$ and $J_2 = 13.7$ K for PBE0 [22]; $J_1 = 13.93$ and $J_2 = 12.76$ K for HSE03 [24]; and $J_1 = 13.00$ and $J_2 = 14.48$ K for HSE06 [14]. The h-DFT results closely match experiment; however, h-DFT is not universally accurate, with $J_1 = 9.80$ and $J_2 = 20.5$ K for B3LYP [28]. Previously, Franchini et al. observed a ratio of $J_2/J_1 = 1.1$ from experiment that is well replicated by h-DFT [22]: we obtain similar ratios of 1.12 and 1.13 for PBE0 and PBESol0, respectively. PBE and PBESol, in comparison, give ratios of 1.11 and 0.81, respectively, with the distinctly lower ratio for PBESol arising from an over-stabilisation of AFM(I) that affects J_1.

Using our calculated J_1 and J_2 values, the transition temperature between AFM(II) and PM phases, namely the Néel temperature (T_N), is obtained in the mean-field approximation (MFA) as [24,42,43]:

$$T_N = \frac{S(S+1)}{3} \sum_{l=1,2} (z_l^{\uparrow\uparrow} - z_l^{\uparrow\downarrow}) J_l = 2S(S+1)J_2 \quad (5)$$

and additionally the Curie constant (or Curie–Weiss Temperature), θ, can be obtained as [24,36,43]:

$$\theta = \frac{S(S+1)}{3} \sum_{l=1,2} (z_l^{\uparrow\uparrow} + z_l^{\uparrow\downarrow}) = S(S+1)(4J_1 + 2J_2). \quad (6)$$

The interpretation of these observables is aided by an understanding of the effect any variation in J_1 and J_2 has on the transition temperatures: an increase of 1 K in J_1, which also then reduces J_2 by 1 K (Eq. (4)), results in a decrease (increase) of 17.5 K for T_N

(θ); an increase of 1 K in J_2 decreases both T_N and θ by 17.5 K, with the inverse also applying for decreases in either of the coupling constants.

From our calculations, T_N (θ) is 278.06 (779.33), 291.63 (1015.63), 132.83 (370.54) and 146.24 (404.52) K for PBE, PBESol, PBE0 and PBESol0; the respective experimental values are 116–120 and 424–610 K [9,6,36,39], with error bars of $< 1\%$ for T_N and unstated for θ. Thus, T_N is surprisingly well reproduced with h-DFT, with only a slight overestimate by ~ 20 K; the same is not true for θ, which the MFA clearly underestimates, but quantitative comparison with experiment is hindered by the range of reported values. The only previously reported calculations of T_N using the MFA approach give $T_N = 520$ and 230 K for the PBE and (PBE0-comparable) HSE03 XC functionals, respectively [24]; alternatively, tight-binding theory gives $T_N = 142$ K and $\theta = 643$ K, which is in better agreement with the experimental results reported by Kittel [6] though the coupling constants, of $J_1 = 16.36$ K and $J_2 = 4.04$ K, deviate significantly from experiment.

Given the numerous reports of coupling constants in the literature but the absence of estimates to T_N and θ, we have calculated missing values in Table 1 using an assumption of $S = 5/2$ unless otherwise stated. The LDA and GGA XC functionals consistently overestimate T_N and θ, with a notable exception being the parameterised DFT + U approach, which gives $T_N = 75.25 - 210$ K. In contrast, HF underestimates T_N (75.25 K) and θ (169.75 K), which is due to its tendency for strong electron localisation that consequentially reduces spin coupling. As with our own calculations, the h-DFT approach gives the best agreement with experiment. The use of $S = \mu/2$ in the calculations of Schrön et al. leads to an increase in the discrepancy between theory and experiment; to complement their analysis, the on-site spin density was extracted from our calculations for the Mn^{2+} cation, in order to re-evaluate Eqs. (3)–(6). For us, this improves the match between computational and experimental values of J_1 and J_2, though the resulting T_N and θ are increased by up to 10% (Table 1), which illustrates somewhat the inherent limitations of the MFA approach. Therefore, whilst it is tempting to suggest improvements can be achieved by the use of non-collinear spin in future work, we assume that greater gains are to be made by replacing the MFA with more accurate methods of deriving T_N and θ. As noted in Table 1, Archer et al. report significant improvements in their predictions of T_N when using Monte Carlo (MC) approaches [14], obtaining $T_N = 125$ K for HSE06 rather than 253 K as calculated using the MFA. A more thorough range of simulation techniques, both numerical and analytical, are presented by Fischer et al. [23]: MC and random-phase approximation (RPA) both give underestimates of T_N by > 25 K, whereas the MFA overestimates by only 10 K. Furthermore, Fischer et al. show that including up to the 11th neighbour shell can reduce the difference between experiment and theory further, with T_N reduced from 129 to 122 K. Such approaches are of merit to investigate further, though it is noted that parameterisation of a Heisenberg Hamiltonian for 11th neighbour interactions would perhaps require performing calculations with large supercell models that remain exhaustive on most current computing infrastructures.

4. Conclusions

In summary, the magnetic properties of MnO have been rigorously investigated using the popular PBE and PBESol GGA-DFT methods, and also their respective h-DFT counterparts PBE0 and PBESol0. The GGA approaches do not match experiment, but h-DFT reproduces experimental results for magnetic coupling constants and transition temperatures to a satisfactory degree of accuracy. Generally, it is noted that the solid-state reparameterisation, namely PBESol, proves less accurate than its parent density func-

tional when calculating the structural properties of MnO. The limitations observed when comparing computed coupling constants and transition temperatures to experiment are noted as being inherent to the mean-field approximation, rather than the levels of theory at which energetic quantities are obtained, though variance in the experimental data, especially for θ, also hampers progression.

Appendix A. Supplementary material

Supplementary data associated with this article can be found, in the online version, at https://doi.org/10.1016/j.cplett.2017.10.027.

References

[1] P.W. Anderson, New approach to the theory of superexchange interactions, Phys. Rev. 115 (1959) 2–13.
[2] W.D. Johnston, R.R. Heikes, A study of the LixMn(1-x)O system, J. Am. Chem. Soc. 78 (1956) 3255–3260.
[3] M. O'Keeffe, M. Valigi, The electrical properties and defect structure of pure and chromium-doped MnO, J. Phys. Chem. Solids 31 (1970) 947–962.
[4] W.B. Pearson, A Handbook of Lattice Spacings and Structures of Metals and Alloys: International Series of Monographs on Metal Physics and Physical Metallurgy, fourth ed., Elsevier, 2013.
[5] J.A.M. Paddison, M.J. Gutmann, J.R. Stewart, M.G. Tucker, M.T. Dove, D.A. Keen, A.L. Goodwin, The Magnetic Structure of Paramagnetic MnO (2016).
[6] C. Kittel, Introduction To Solid State Physics, eighth ed., Wiley, New York, 2004.
[7] W.L. Roth, Magnetic Structures of MnO, FeO, CoO, and NiO, Phys. Rev. 110 (1958) 1333–1341.
[8] A.L. Goodwin, M.G. Tucker, M.T. Dove, D.A. Keen, Magnetic structure of MnO at 10 K from total neutron scattering data, Phys. Rev. Lett. 96 (2006) 47209.
[9] B. Morosin, Exchange striction effects in MnO and MnS, Phys. Rev. B 1 (1970) 236–243.
[10] A.K. Cheetham, D.A.O. Hope, Magnetic ordering and exchange effects in the antiferromagnetic solid solutions Mn x Ni 1 x O, Phys. Rev. B 27 (1983) 6964–6967.
[11] H. Shaked, J. Faber, R.L. Hitterman, low-temperature magnetic structure of MnO: a high-resolution neutron-diffraction study, Phys. Rev. B 38 (1988) 11901–11903.
[12] F. Corà, M. Alfredsson, G. Mallia, D.S. Middlemiss, W.C. Mackrodt, R. Dovesi, R. Orlando, The Performance of Hybrid Density Functionals in Solid State Chemistry, Springer, Berlin Heidelberg, 2004.
[13] W.A. Harrison, Heisenberg exchange in the magnetic monoxides, Phys. Rev. B - Condens. Matter Mater. Phys. 76 (2007) 054417.
[14] T. Archer, C.D. Pemmaraju, S. Sanvito, C. Franchini, J. He, A. Filippetti, P. Delugas, D. Puggioni, V. Fiorentini, R. Tiwari, P. Majumdar, Exchange interactions and magnetic phases of transition metal oxides: Benchmarking advanced ab initio methods, Phys. Rev. B 84 (2011) 115114.
[15] K. Terakura, T. Oguchi, A.R. Williams, J. Kübler, Band theory of insulating transition-metal monoxides: Band-structure calculations, Phys. Rev. B 30 (1984) 4734–4747.
[16] G.A. Sawatzky, J.W. Allen, Magnitude and origin of the band gap in NiO, Phys. Rev. Lett. 53 (1984) 2339–2342.
[17] S. Hüfner, Electronic structure of NiO and related 3d-transition-metal compounds, Adv. Phys. 43 (1994) 183–356.
[18] T. Bally, G.N. Sastry, Incorrect dissociation behavior of radical ions in density functional calculations, J. Phys. Chem. A 101 (1997) 7923–7925.
[19] Y. Zhang, W. Yang, A challenge for density functionals: Self-interaction error increases for systems with a noninteger number of electrons, J. Chem. Phys. 109 (1998) 2604–2608.

[20] M. Lundberg, P.E.M. Siegbahn, Quantifying the effects of the self-interaction error in DFT: When do the delocalized states appear?, J Chem. Phys. 122 (2005) 224103.

[21] S.L. Dudarev, G.A. Botton, S.Y. Savrasov, C.J. Humphreys, A.P. Sutton, Electron-energy-loss spectra and the structural stability of nickel oxide: An LSDA+U study, Phys. Rev. B 57 (1998) 1505–1509.

[22] C. Franchini, V. Bayer, R. Podloucky, J. Paier, G. Kresse, Density functional theory study of MnO by a hybrid functional approach, Phys. Rev. B 72 (2005) 045132.

[23] G. Fischer, M. Däne, A. Ernst, P. Bruno, M. Lüders, Z. Szotek, W. Temmerman, W. Hergert, Exchange coupling in transition metal monoxides: Electronic structure calculations, Phys. Rev. B 80 (2009) 14408.

[24] A. Schrön, C. Rödl, F. Bechstedt, Energetic stability and magnetic properties of MnO in the rocksalt, wurtzite, and zinc-blende structures: Influence of exchange and correlation, Phys. Rev. B 82 (2010) 165109.

[25] J.P. Perdew, M. Ernzerhof, K. Burke, Rationale for mixing exact exchange with density functional approximations, J. Chem. Phys. 105 (1996) 9982–9985.

[26] M. Marsman, J. Paier, A. Stroppa, G. Kresse, Hybrid functionals applied to extended systems, J. Phys. Condens. Matter 20 (2008) 064201.

[27] C. Franchini, R. Podloucky, J. Paier, M. Marsman, G. Kresse, Ground-state properties of multivalent manganese oxides: Density functional and hybrid density functional calculations, Phys. Rev. B 75 (2007) 195128.

[28] X. Feng, Electronic structure of MnO and CoO from the B3LYP hybrid density functional method, Phys. Rev. B 69 (2004) 155107.

[29] G. Kresse, J. Furthmüller, Efficiency of ab-initio total energy calculations for metals and semiconductors using a plane-wave basis set, Comp. Mater. Sci. 6 (1996) 15–50.

[30] G. Kresse, D. Joubert, From ultrasoft pseudopotentials to the projector augmented-wave method, Phys. Rev. B 59 (1999) 1758–1775.

[31] G. Kresse, J. Furthmüller, Efficient iterative schemes for ab initio total-energy calculations using a plane-wave basis set, Phys. Rev. B 54 (1996) 11169–11186.

[32] J.P. Perdew, K. Burke, M. Ernzerhof, Generalized gradient approximation made simple, Phys. Rev. Lett. 77 (1996) 3865–3868.

[33] C. Adamo, V. Barone, Toward reliable density functional methods without adjustable parameters: The PBE0 model, J. Chem. Phys. 110 (1999) 6158–6170.

[34] J.P. Perdew, A. Ruzsinszky, G.I. Csonka, O.A. Vydrov, G.E. Scuseria, L.A. Constantin, X. Zhou, K. Burke, Restoring the density-gradient expansion for exchange in solids and surfaces, Phys. Rev. Lett. 100 (2008) 136406.

[35] W. Jauch, M. Reehuis, Electron density distribution in paramagnetic and antiferromagnetic MnO: A γ-ray diffraction study, Phys. Rev. B 67 (2003) 184420.

[36] M.E. Lines, E.D. Jones, Antiferromagnetism in the face-centered cubic lattice. II. Magnetic properties of MnO, Phys. Rev. 139 (1965) A1313–A1327.

[37] G. Pepy, Spin waves in MnO; from 4 K to temperatures close to TN, J. Phys. Chem. Solids 35 (1974) 433–444.

[38] M. Kohgi, Y. Ishikawa, Y. Endoh, Inelastic neutron scattering study of spin waves in MnO, Solid State Commun. 11 (1972) 391–394.

[39] J.J. Banewicz, R.F. Heidelberg, A.H. Luxem, High temperature magnetic susceptibilities of MnO, MnSe and MnTe, J. Phys. Chem. 65 (1961) 615–617.

[40] R. Logemann, A.N. Rudenko, M.I. Katsnelson, A. Kirilyuk, Exchange interactions in transition metal oxides: the role of oxygen spin polarization, J. Phys. Condens. Matter 29 (2017) 335801.

[41] M.D. Towler, N.L. Allan, N.M. Harrison, V.R. Saunders, W.C. Mackrodt, E. Aprà, Ab initio study of MnO and NiO, Phys. Rev. B 50 (1994) 5041–5054.

[42] D. Bloch, R. Maury, Uniaxial stress experiments and magnetoelastic interactions in manganese oxide, Phys. Rev. B 7 (1973) 4883–4888.

[43] N.W. Ashcroft, N.D. Mermin, Solid State Physics, HRW International Ed., Holt, Rinehart and Winston, 1976.